

A Validation/Uncertainty Quantification Analysis of a 1.5 MW Oxy-Coal Fired Furnace

Oscar H. Diaz-Ibarra, Jennifer Spinti, Andrew Fry, Benjamin Schroeder, Jeremy N. Thornock, Benjamin Issac, Derek Harris, Michal Hradisky, Sean Smith, Eric Eddings, Philip J. Smith

Institute for Clean and Secure Energy, University of Utah, Salt Lake City, UT

Abstract

A validation and uncertainty quantification study of a 1.5 MW oxy-coal fired furnace is presented. In this study, a consistency analysis approach was applied to experimental and simulation results for eight quantities of interest: thermocouple measurements in five locations down the length of the furnace and three radiometer measurements in the first three sections of the furnace. Instrument models were devised for both the thermocouples and radiometer measurements so that experimental and simulation data could be compared. A total of six parameters were tested through the consistency analysis. In the simulations, two parameters were tested, the thermal wall resistance and a devolatilization parameter. In the instrument models, four parameters were tested: the emissivity of the thermocouple in the thermocouple model and, the emissivity of the wall opposite to the radiometer in the radiometer model.

Nomenclature

ε	Emissivity	[-]
$q_{incident}$	Incident radiation	[W/m ²]
σ	Stefan-Boltzmann constant	5.670373 e-8 [W/m ² /K ⁴]
R	Thermal resistance	[W/m ² /K]
T	Temperature	[K]
k_i	Thermal conductivity	[W/m/K]
Δx_i	Layer thickness	[m]
v_{hiT}	Devolatilization parameter	[-]
V_f	Ultimate volatile yield	[-]
T_p	Particle temperature	[K]
V	Volatile yield	[-]
A	Pre-exponential factor	[1/s]
E	Activation temperature	[K]
σ_a	Distribution's standard deviation	[K]
Z	$\max(-4.0, \min(\sqrt{2.0} * \operatorname{erfinv}(1.0 - 2.0 * (V_f - V)/v_{hiT}, 4.0))$	
$q_{removal}$	Heat removed	[W/cell/m ²]

k	Thermal conductivity over thickness of the thermocouple	[W/m ² /K]
\bar{L}		
h	Heat transfer coefficient on the thermocouple	[W/m ² /K]
<i>solid_angle</i>	Solid angle for the radiometer	
I	Intensity	[W/m ²]
I_b	$\frac{\sigma T_{gas}^4}{\pi}$	[W/m ²]
k_{i+1}	Absorption coefficient	[1/m]
Δx	Resolution	[m]
N_r	Number of rays	
I_o	Intensity at the wall oppose to radiometer	[W/m ²]

Subscripts

<i>cold_target</i>	Heat flux gauge
<i>tc</i>	Thermocouple instrument
<i>gas</i>	Gas
<i>shell</i>	Shell
<i>w</i>	Wall
<i>p</i>	Particle

1. Introduction

The Carbon Capture Multidisciplinary Simulation Center (CCMSC) (<http://ccmsc.utah.edu>), at the University of Utah is demonstrating the use of exascale computing with verification, validation, and uncertainty quantification as a means of accelerating deployment of low cost, low emission coal-fired power generation technologies. This effort employs a [hierarchical validation](#) approach to obtain simultaneous consistency between a set of selected experiments at different scales embodying the key physics components (large eddy simulations, multiphase flow, particle combustion and radiation) of a full-scale, oxy-fired boiler. This paper presents validation and uncertainty quantification (VUQ) results for one of the selected datasets, a suite of oxycoal-fired experiments conducted in the L1500 (a 1.5 MW furnace at the University of Utah). The VUQ method used was a consistency analysis. With this method, regions of consistency between experimental and simulation data were determined. Details about the L1500 furnace and the experimental data can be found in the accompanying paper by Fry et al. entitled “Pilot-scale Investigation of Heat Flux and Radiation from an Oxy-coal Flame” This paper focuses on the L1500 simulations, the collection/processing of the simulation data, and the VUQ consistency analysis.

2. Methodology

To perform a VUQ analysis, the quantity (or quantities) of interest (QOI) and the system parameters (scenario, model, numerical) that have a first order impact on the QOI are identified. In this experimental dataset, the QOIs all relate to heat flux:

wall temperature, heat flux measured by narrow-angle radiometers, and wall heat flux. For this initial analysis, a two-parameter study was selected due to constraints of time and computer resources.

2.1 Design of Experiments

The two parameters explored in this study were a devolatilization model parameter and a scenario parameter related to thermal resistance in the wall heat transfer model. These parameters were selected based on prior experience and a desire to have one model parameter that was investigated at all relevant levels of the validation hierarchy.

Within the simulation tool, the models for coal particle physics include a devolatilization model that is presented in equations (1) and (2). In this model, the ultimate volatile yield is determined by the function shown in Equation (1):

$$V_f = \frac{v_{hiT}}{2} \left(1 - \tanh \left((b + c * v_{hiT}) * \frac{590 - T_p}{T_p} + (d + e * v_{hiT}) \right) \right) \quad (1)$$

$$\frac{dV}{dt} = \begin{cases} A * \exp \left(-\frac{E + \sigma_a * Z}{T_p} \right) (V_f - V), & \text{if } V_f - V \leq 0 \\ 0, & \text{else} \end{cases} \quad (2)$$

In equation (1), the parameters b, c, d and e were fitted using data from the Chemical Percolation Devolatilization (CPD) model [1]. The parameter v_{hiT} was explored in this VUQ analysis in the range of 0.5–0.9. The volatile yield was used in equation (2) to compute the rate of devolatilization. More detailed information about this new devolatilization model can be found in [2].

A scenario parameter called the “effective thickness” is related to the thermal resistance used in the one-dimensional (1D) wall heat transfer model equation shown in equation (3). The walls of the L1500 furnace consist of one layer of refractory material and three insulation layers for a total wall thickness of 0.34 m. The 1D heat transfer equation for this multilayer wall is given in equation (4). Finally, the “effective thickness” scenario parameter, $\frac{1}{R}$, is presented in equation (5). The selected range for this parameter was 0.1–0.4 based on uncertainty in the wall emissivity and on temperature dependence of the thermal conductivity.

$$\varepsilon(q_{incident} - \sigma T_w^4) = R(T_w - T_{shell}) \quad (3)$$

$$(q_{incident} - \sigma T_w^4) = \frac{1}{\varepsilon \sum_{i=1}^n \frac{\Delta x_i}{k_i}} (T_w - T_{shell}) \quad (4)$$

$$\frac{1}{R} = \varepsilon \sum_{i=1}^n \frac{\Delta x_i}{k_i} \quad (5)$$

A total of eight cases were run for this analysis. Latin hypercube sampling was used to generate the sets of parameter values that best represented the two-dimensional parameter space. This eight-case design of experiments is presented in Table 1.

Table 1. Design of experiments for the VUQ analysis.

Case	v_{hiT}	$\frac{1}{R}$ [m ² k/W]
1	0.7738	0.10
2	0.5228	0.14
3	0.827	0.20
4	0.6019	0.23
5	0.729	0.25
6	0.6737	0.32
7	0.88022	0.35
8	0.5503	0.37

For the eight cases presented in Table 1, the following simulation tool, geometry and operating conditions were used.

2.2 Simulation Tool

The simulations were performed with Arches, a component of the Uintah software suite [3]. Uintah is a solver for partial differential equations on structured grids using hundreds to thousands of processors.

In Arches, the turbulent flow is resolved by the filtered Navier-Stokes equations. In this Large Eddy Simulation (LES) approach, the large scales are resolved, and the subgrid scales are modeled with the dynamic Smagorinsky model. For the LES simulations described in this paper, first order discretization in time and a wall upwind convection scheme were used.

The solid phase was modeled using the direct quadrature method of moments (DQMOM) with three environments. The internal coordinates were the raw coal mass, the char mass, the enthalpy of the particle, and the velocity of the particle (in x, y, and z). In addition, the weights for the three environments were solved. An upwind discretization scheme was used to solve the equations for the internal coordinates and for the weights. The particle phase was coupled with the gas phase through source terms in the equations for momentum, heat and mass. More detail about the DQMOM implementation in Arches is presented in [4]. The coal particle physics models included the devolatilization model discussed above and the Shaddix and Murphy char oxidation model [5].

The gas-phase reactions in the system were modeled using a three-stream mixture fraction approach. The three streams are recycled flue gas (m_{RFG}), oxygen (m_{O_2}),

and coal off gas (m_c). The mixture fractions based on these three streams are defined in equations (6), (7) and (8).

$$\eta_{p,gas} = \frac{m_{RFG}}{m_{RFG}+m_{O_2}} \quad (6)$$

$$\eta_p = \frac{m_{RFG}}{m_{RFG}+m_{O_2}+m_c} \quad (7)$$

$$\eta_c = \frac{m_c}{m_{RFG}+m_{O_2}+m_c} \quad (8)$$

Transport equations were solved for η_c and $\eta_{p,gas}$; η_p was computed from the other two mass fractions. A lookup table based on equilibrium chemistry assumptions was tabulated a priori as a function of these three mixture fractions and of the system enthalpy.

The discrete ordinates (DO) method was used to compute radiation in the simulation. For the cases in this paper, S8 quadrature, representing 40 discrete directions, was used. The radiation equations were solved every 20 iterations.

2.3 Geometry and Computational Domain

The L1500 reactor is 15.5 m long with a 1x1 m² transversal area as shown in Figure 1. It is divided into 10 sections, and each section has several ports through which a variety of measurements can be taken. The L1500 has a swirling burner that can operated in a range of modes from 0% swirl, where completely straight flow can be achieved, to 100% swirl, where flow with a 32 m/s tangential velocity and 22 m/s axial velocity can be obtained. The L1500 can be operated in air-fired or oxy-fired modes and can burn solid, liquid, or gaseous fuels. In oxy-fired mode, recycled flue gas (RFG) is brought from the exit of the convective section back into the burner's primary/secondary oxidant registers. Oxygen is supplied to the secondary and primary RFG streams just prior to entering the burner. For the experiments used in this validation study, coal was fed with the primary stream at a rate of 0.0324 kg/s in order to produce 1 MW of heat. More information about this reactor and burner can be found in [6] and [7].

The computational geometry for the entire furnace is presented in Figure 2. The reactor has eight sets of water-cooled tubes that remove heat from the first four sections. Additionally, there is a water-cooled steel grid at the furnace exit to reduce the temperature of the combustion gases prior to entering the convection section. Also seen in Figure 2 are the burner quarl, the geometry of the furnace exit, and the 10 cm step up in the bottom of the furnace between sections 4 and 5.



Figure 1: Photo of the L1500 reactor located at the Industrial Combustion And Gasification Research Facility [8].

Several simulations using the entire furnace geometry at a resolution of 16 mm were carried out for the 0% swirl case. From these simulations, it was clear that after section 6, gas temperatures, velocities and chemical compositions were relatively constant. The computational geometry was shortened to 7 m and additional simulations were run. Simulation results from the 7 m simulation were compared with results from the 15.5 m simulation and the differences were minimal. Hence, for subsequent simulations, the computational geometry was shortened to 7 m. The impact of mesh resolution on simulation results was also tested by performing a simulation with 12 mm resolution. While the differences in the wall temperature profiles for the 12 mm and 16 mm resolution cases were small, there were larger differences in gas temperatures near the burner. Therefore, a 12 mm resolution has selected for the VUQ analysis.

The shortened geometry of the L1500 with a 12 mm resolution is presented in Figure 3; this geometry includes the cooling tubes and the step. The surface area of the cooling tubes in the computational mesh was adjusted to match the actual surface of the tubes. With this new geometry, comparisons could be made with most of the experimental data, including narrow-angle radiometer measurements in sections 1, 2, and 3; wall temperatures in sections 1, 2, 3, 4 and 6; gas compositions in sections 4, 5, and 6; and total heat flux in sections 1, 2, and 3. Gas composition data from sections 7, 8, 9 and 10 could not be used, but, the gas composition was fairly constant through these sections.

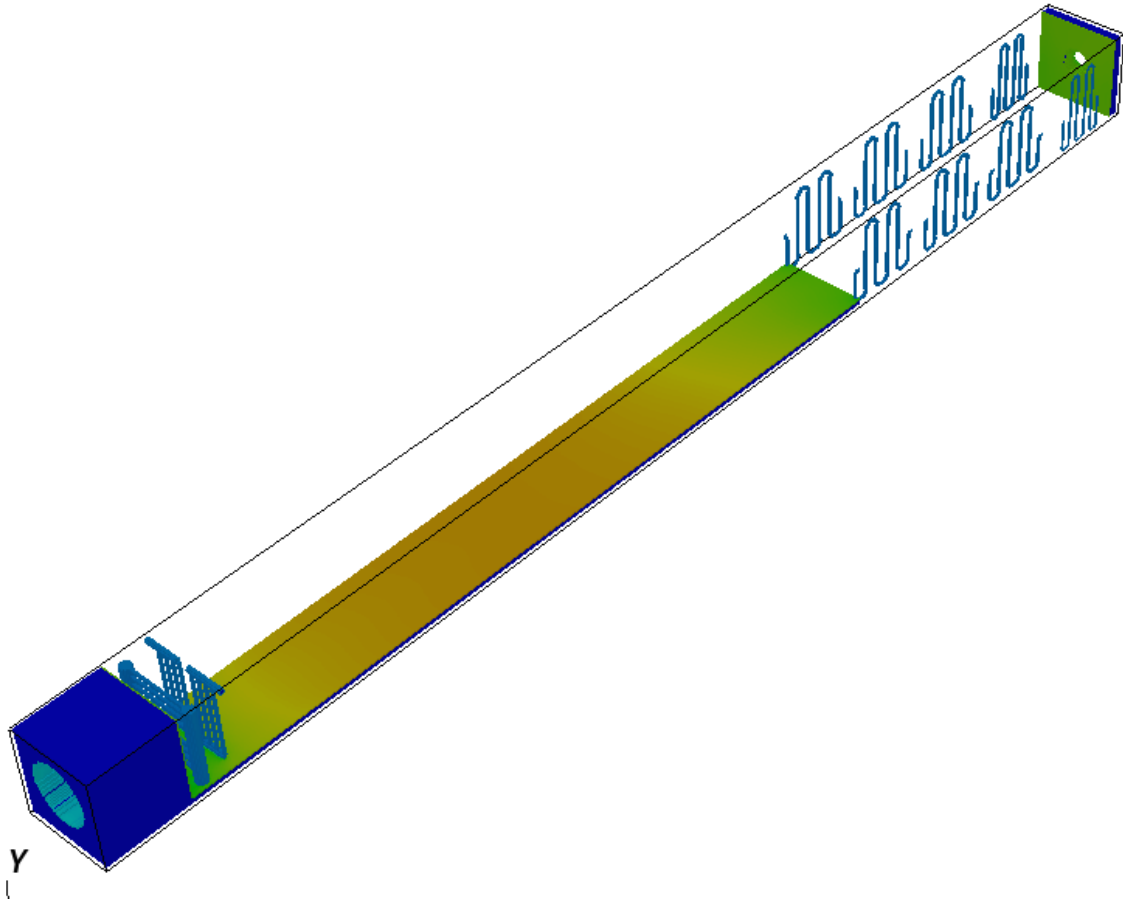


Figure 2: Computational geometry for the L1500 showing the eight sets of cooling tubes, the cooling grid, the burner quarl, the step after section 4, and the exit.

The L1500 simulations were run on two linux machines: Ash, a machine owned by the Institute for Clean and Secure Energy and operated by the Center for High Performance Computing at the University of Utah, and Syrah, a machine operated by Lawrence Livermore National Laboratory. With a 12 mm mesh resolution (mesh is uniform and structured), the computational domain had 4,463,448 cells. The simulations were run on 464 cores long enough to obtain 20 s of physical time. On Syrah, this required 80 hours of run time.

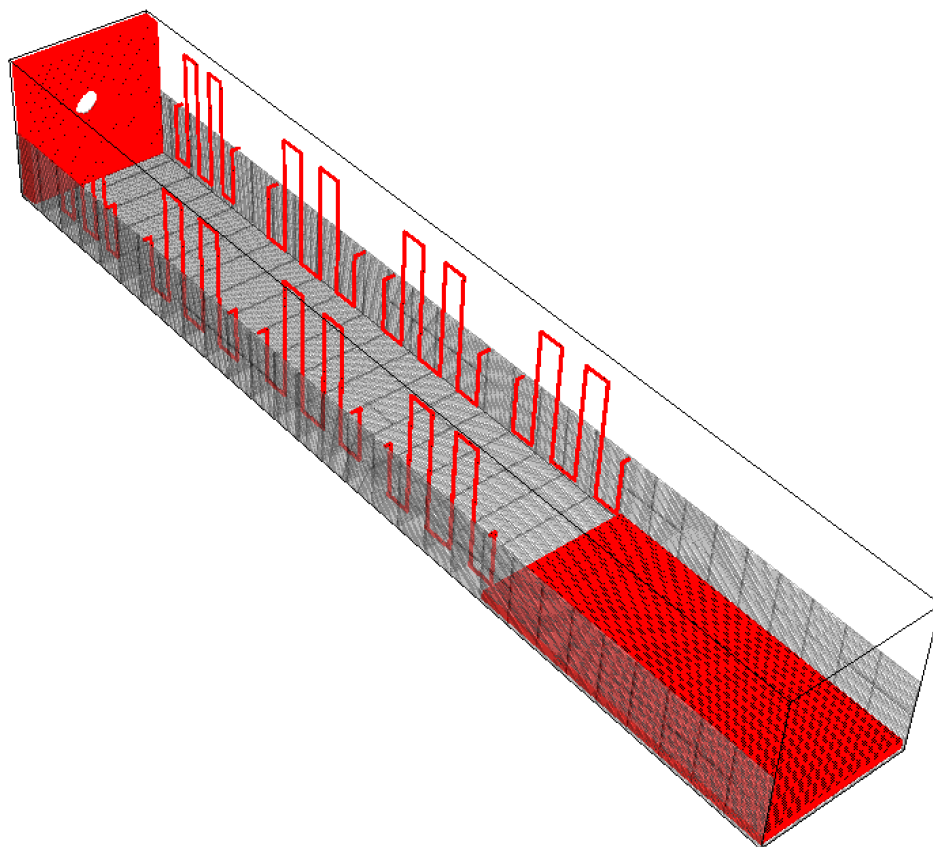


Figure 3: Shortened geometry for the L1500 simulations including the quarl, the eight sets of cooling tubes, and the step change in the reactor floor.

2.4 Coal Characterization

A Sufco Utah coal was used in the experimental campaign. The ultimate analysis for this coal is presented in Table 2.

Table 2. Ultimate analysis for the Sufco Utah Coal. Data are averaged and normalized from the analysis of five samples.

Coal	% Mass
C	66.89
H	4.51
N	1.17
S	0.36
O	13.6
Ash	7.88
H ₂ O	5.58
HHV [J/kg]	27364.93

To determine the particle size distribution (PSD) of the Sufco coal, the bags of coal to be burned during the experimental campaign were sampled at different depths. Both a sieving analysis and a Beckman-Coulter diffraction analysis were performed on the collected samples. As seen in Figure 4, data from both methods were fitted to a Rosin-Rammler distribution. From this analysis, it was concluded that the PSD distribution could be approximated by three particle sizes: $15\ \mu\text{m}$, $60\ \mu\text{m}$, and $200\ \mu\text{m}$, with mass weights of 57.4%, 26.2% and 16.4% respectively. Assuming that the particle velocities were the same as the gas velocity, these mass weights were converted to particles per cubic meter using a coal density of $1300\ \frac{\text{kg}}{\text{m}^3}$ and the volume corresponding to each particle size. Thus, the inputs to DQMOM were the number of particles per m^3 for each of the three particles size.

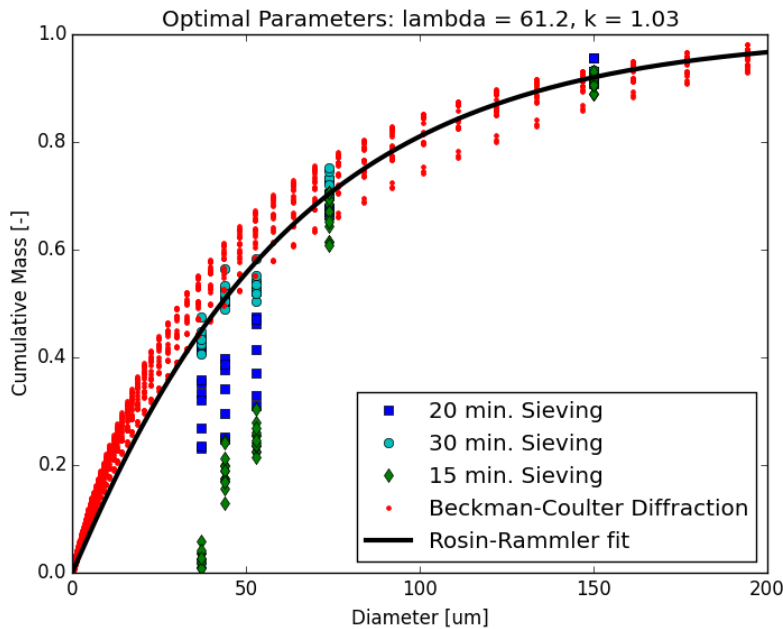


Figure 4: Experimental PSD and fitted Rosin-Rammler PSD. Sieving was performed for different times to determine the effect on the resulting PSD. Based on this analysis, only the 30-minute sieving data was used for the Rosin-Rammler fit.

2.5 Operating Conditions

An experimental campaign was carried out for a week in the L1500 where both 0% swirl and 100% swirl operating conditions were tested. The L1500 operating parameters that were used as inputs to the Arches simulations are shown in Table 3. These inputs were computed from the mass flow of the RFG to the primary and secondary registers, the oxygen mass flow to the primary and secondary inlets, the coal mass flow rate, the gas temperatures for each of these streams, and the composition of RFG. All of these parameters were recorded and controlled during the experimental campaign. For the 0% swirl operating condition, a constant

velocity profile at the tip of the burner was assumed for the primary and secondary oxidant streams.

Table 3. L1500 operating conditions used as inputs for Arches simulations.

Stream	Mass flow [kg/s]	Temperature [K]
Coal (ash and moisture free)	0.0324	338
Primary	0.0688	338
Secondary	0.2995	500
Mass Fraction	Primary	Secondary
O ₂	0.1739	0.2385
CO ₂	0.6746	0.6245
H ₂ O	0.1043	0.0966
SO ₂	0.0020	0.0018
N ₂	0.0450	0.0416

These operating conditions were generally stable during the experiment. However, there was an air leak in the RFG stream as evidenced by the outlet CO₂ concentration being lower than expected. To compensate for this air leak in the simulations, an overall mass balance was performed on the furnace. The leaked air and the coal's moisture were included in the compositions of the RFG flow shown in Table 3.

During the experimental campaign, radiative heat flux was measured through the center port of sections 1, 2, and 3 using a narrow-angle radiometer. A cold plate serving as a heat flux gauge was installed in the port opposite from the radiometer to measure total heat flux to the wall and to provide a known boundary condition for the radiometer measurements. In practice, the cold surface became coated with radiating particles, introducing uncertainty into the radiometer measurement. Mass flow rates and inlet/outlet temperatures of the water flowing through the cold plate heat flux gauges were recorded. Mass flow rates and inlet/outlet temperatures of the water flowing through the cooling tubes were measured as well. "Wall" temperature measurements were taken in sections 1, 2, 3, 4, 6, 7 and 8 using Type B thermocouples encased in ceramic sheaths that were then inserted into small holes in the furnace ceiling located in the middle of each section (see Figure 5). Each sheath was inserted until it was flush with the inside wall of the furnace. Gas phase composition was continuously measured at the furnace outlet. In addition, a mobile gas probe was used to record centerline and radial gas phase compositions between sections 4 and 10. Finally, detailed shell temperature profiles were taken of each of the 10 sections.

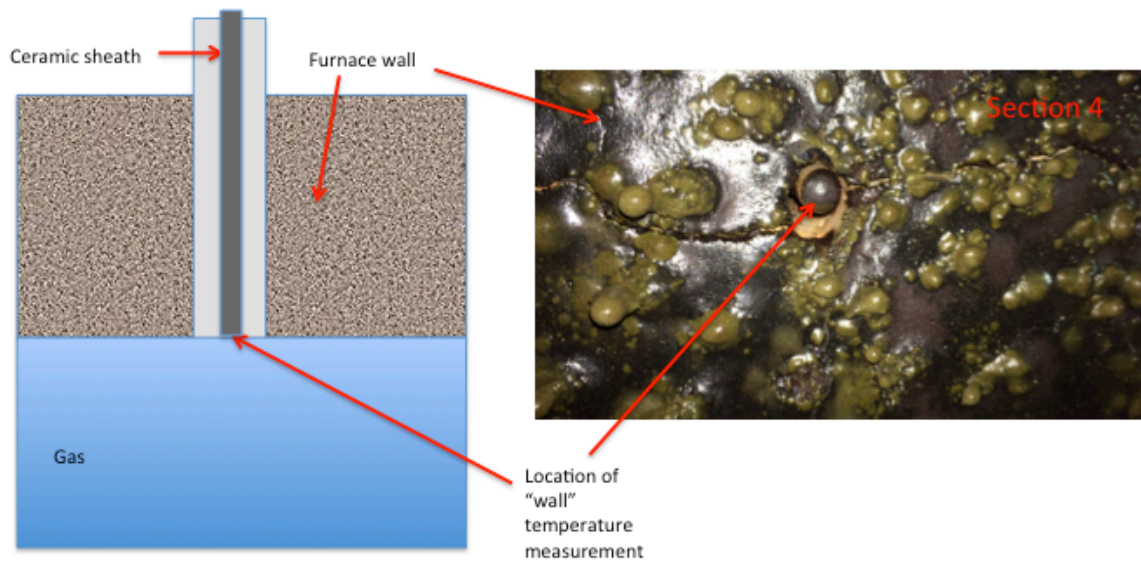


Figure 5: Thermocouple placement in furnace wall. Section 4 is shown but the placement is similar for all thermocouple measurements.

In scoping simulations, it was determined that simulation results (specifically radiative heat flux and wall temperatures) were not sensitive to the shell temperature of the furnace. Therefore, constant values were used for each of the four sides of the furnace. Table 4 presents the values of shell temperature used in the simulations.

Table 4. Shell temperatures averaged over all measurements made on a side.

Location	Shell Temperature (K)
Quarl	434
Main chamber south side	362
Main chamber north side	396
Main chamber bottom side	362
Main chamber top side	427.2

2.6 Heat Removal by the Cooling Tubes

Figure 6 shows the heat removed by cooling tubes 1 and 2 (both in section 1) as a function of time during the last day of the experiment. The quantity of heat removed generally decreased until the burner was switched from 0% to 100% swirl (represented by the vertical black line at 109 hours in the figure). After the brief jump with the change in swirl, the heat removal continued its general decline. This behavior was due to ash deposition on the cooling tube surface. However, sometimes the heat removal increased, which could have been due to ash material falling from the tubes. Figure 7 shows a photo of one set of cooling tubes after the experiment. In this photo, it can be seen that the ash layer on the tubes is not uniform and there are some locations where the ash material has fallen off.

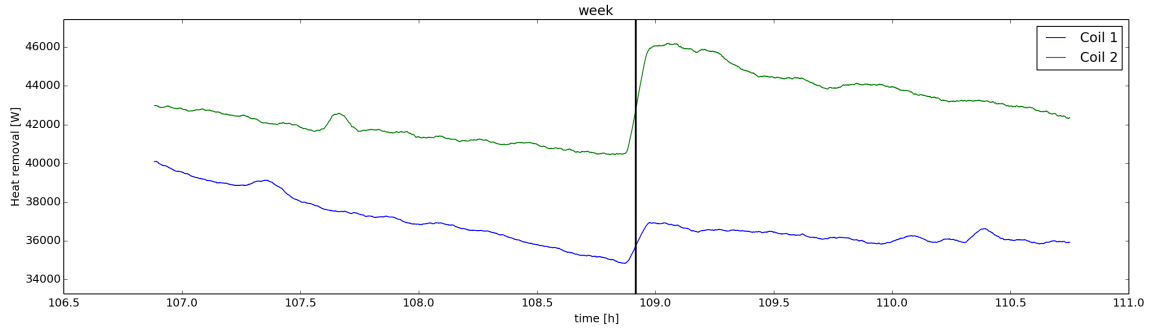


Figure 6: Heat removal by cooling tubes 1 and 2. The vertical line represents the point where operating conditions were switched from 0% swirl to 100% swirl.



Figure 7: Cooling tubes after the experiment.

Heat removal by the cooling tubes is an important parameter that ideally would be computed and then compared to experimental values as part of the VUQ analysis. However, Arches does not currently have a model to compute ash deposition and the resultant changes in emissivity and conductivity of the cooling tubes. Additionally, ash deposition is a slow process in comparison with an LES simulation. A preliminary simulation was run assuming clean tubes. However, temperature and heat flux profiles from the simulation did not agree with the experimental values. Therefore, it was decided that heat removal by the cooling tubes would be used as an input parameter instead of an output.

To include the heat removed as an input parameter, an energy balance, given in equation (9), was performed on each set of cooling tubes. The parameter R , defined in equation (5), was computed using equation (10). Equation (9) assumes a constant heat removal along the length of each set of cooling tubes. The value for q_{removal} , the total heat removal for a set of tubes, was obtained from the experimental data. Since the diameter of the tubes was equal to the cell size, this value was divided by the

total number of cells representing each set of tubes in the computational domain to obtain the heat removal per cell.

$$R(T_w - T_{shell}) = q_{removal} \quad (9)$$

$$R = \frac{q_{removal}}{(T_w - T_{shell})} \quad (10)$$

Because the parameter R (a strong function of ash deposition along the entire tube length) was not controlled in the experiment, experimental data from a small window in time were used for the VUQ analysis. By choosing a small window, the ash layer on the cooling tubes was assumed to be constant and R was computed using equation (10). For future studies, this parameter will be included as one of the variable parameters in the VUQ analysis.

2.7 Quantities of Interest for the VUQ Analysis

As noted previously, the QOIs for this study were related to the radiative heat flux in the furnace under oxycoal firing conditions. Specifically, the QOIs were “wall” temperatures measured by thermocouples in sections 1, 2, 3, 4, and 6; radiative heat flux measured by the narrow-angle radiometer in sections 1, 2, and 3; and the total heat flux at the wall measured in sections 1, 2, and 3. These data were used in the VUQ analysis that follows.

2.8 Description of VUQ Approach

The VUQ methodology employed for this study was a consistency measure analysis referred as bounds to bounds consistency. This methodology was developed by Michael Frenklach and Andrew Packard at the University of California Berkeley [2]. The basic concept of this consistency analysis boils down to comparing modeling outputs with experimental data using equation (11). In equation (11), the discrepancy u_e between the model data ($y_{m,e}(\mathbf{x})$) and the experimental data (y_e) is computed. If u_e is lower than the error in the experimental measurement, the simulation and experimental data are consistent. If the data are not consistent, the simulation scientist must reassess whether the models and model parameter ranges are appropriate for the system being studied and the experimentalist must reevaluate the experimental methods and data to see if there are unaccounted for errors that might increase the uncertainty in the measurement. As discussed in Section 3, identifying regions of consistency may help reduce the uncertainty in the parameter space.

$$|y_{m,e}(\mathbf{x}) - y_e| \leq u_e \quad (11)$$

3 VUQ Results

Here, the consistency analysis is applied to thermocouple and radiometer measurements. In order to compare experimental data and simulation data, instrument models for the thermocouple and the radiometer were devised.

3.1 Temperature Measurement Analysis

The instrument model for the thermocouple in the ceramic sheath was shown schematically in Figure 5. In the instrument model, the energy equation (12) was solved for T_{tc} , the temperature that would be measured by the thermocouple shown in Figure 5 given the simulated conditions of the furnace. The value for T_{tc} is then directly comparable to the thermocouple temperature measured experimentally.

$$\varepsilon_{tc}(q_{incident} - \sigma T_{tc}^4) + \frac{k}{L}(T_{tc} - T_{shell}) + h(T_{gas} - T_{tc}) = 0 \quad (12)$$

For a given case, the incident radiation $q_{incident}$ and the gas temperature T_{gas} in equation (12) were obtained from the simulation by extracting data at the thermocouple's location and averaging the data over two seconds. The thermal resistance $\frac{k}{L}$ of the thermocouple was obtained from product literature. The value of T_{shell} was obtained from Table 4 for the "Main chamber top side." The heat transfer coefficient h was set to $4.0 \frac{W}{m^2 \cdot K}$. Because the surface emissivity ε_{tc} had a strong effect on measured temperature, it was varied between 0–1 in the instrument model. With all these values set, equation (12) was used to solve for T_{tc} . This process was repeated using results from each of the eight simulations presented in Table 1.

Three dimensional surfaces (e.g. surrogate models) for T_{gas} and $q_{incident}$ were constructed with a Gaussian Process [9] using the data obtained from the eight simulations. The set of surrogate models created for T_{gas} is shown in Figure 8, one for each section. The measurement location in each section was the middle of the ceiling. The black dots in the plots are the T_{gas} values from the eight simulations.

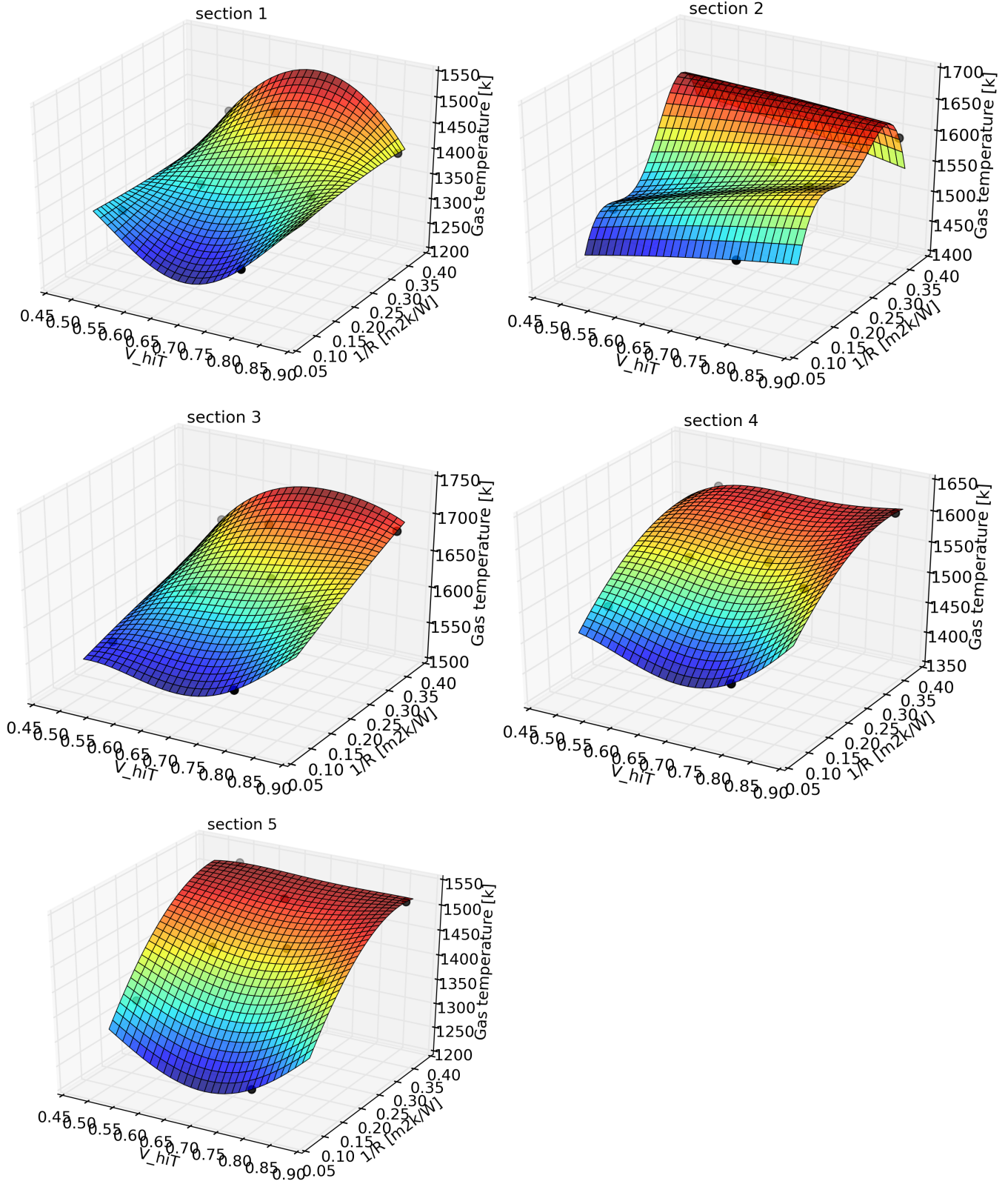


Figure 8: Gas temperature at five different positions on the ceiling of the L1500. The black dots correspond to simulation data; the surface represents the surrogate model.

The behavior of the two parameters is similar for sections 1, 3, 4 and 5 but is different for section 2. This behavior may be related to the recirculation patterns present in section 2. From this figure, it can be seen that the gas temperature increases as $\frac{1}{R}$ increases because the heat lost through the wall is decreasing. The gas temperature also increases with v_{hiT} , but the surface in section 2 has an odd maximum, possibly due to recirculation.

Figure 9 shows the simulation and experimental data with their associated uncertainty ranges at the five measurement locations. For a given location and case (e.g. $q_{incident}$ and T_{gas} fixed) in Figure 9, the range in the thermocouple temperature ($\pm 100K$) results from varying ε_{tc} from 0.2 to 1.0. For a given location considering all cases, the overall range of computed temperatures ($\pm 500K$) is determined by varying $q_{incident}$ and T_{gas} . Since the instrument model shown in equation (12) is most sensitive to $q_{incident}$ and T_{gas} and since $q_{incident}$ and T_{gas} are functions of $\frac{1}{R}$ and v_{hiT} , the three parameters explored for the thermocouple model in the VUQ analysis were $\frac{1}{R}$, v_{hiT} , and ε_{tc} . Figure 9 presents the range of temperatures values obtained at each location by varying these three parameters. Also shown in the figure are the experimental data averaged over a five-minute window with the range determined by the maximum and minimum values of the temperature in that window.

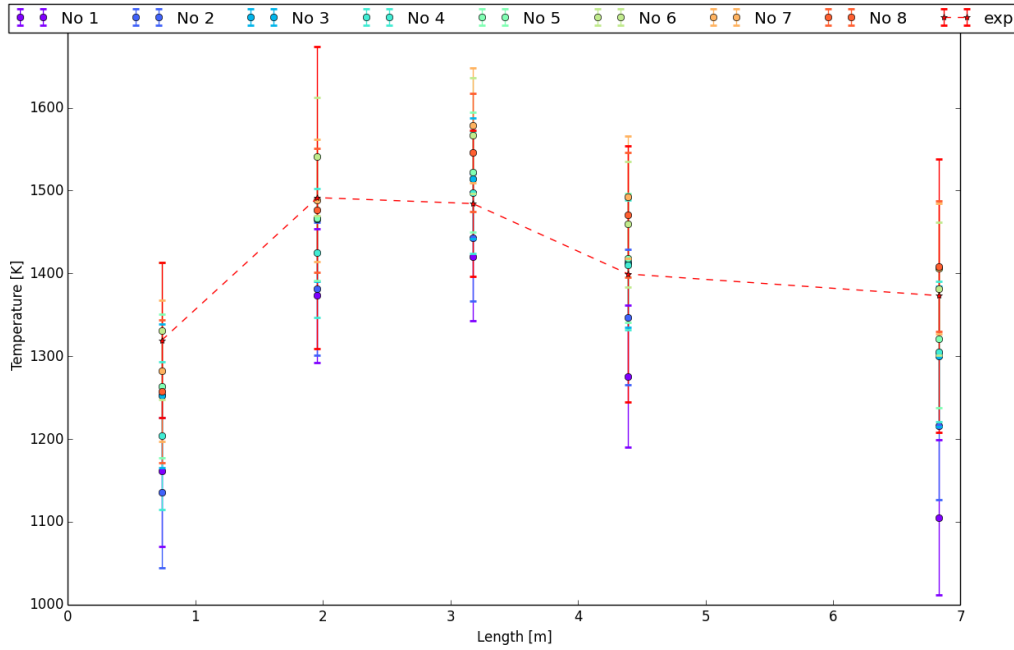


Figure 9: Thermocouple temperature at five positions along the L1500. The simulation error bars correspond to emissivities of 1 and 0.2 for the eight cases presented in Table 1. The red line corresponds to the experimental data.

3.2 Radiometer Measurement Analysis

A narrow-angle radiometer was used to measure the radiative heat flux in sections 1, 2 and 3 in the L1500. The instrument model for the radiometer used a reverse-Monte Carlo ray tracing approach to compute the radiative heat flux by summing up the radiative intensities over all the rays comprising the field of view of the radiometer as seen in equation (13). The radiative intensity in each solid angle, I_r , was computed with equation (14). For this analysis, $N_r = 1$.

$$q = \text{solid_angle} \frac{1}{N_r} \sum_{r=1}^{N_r} I_r \cos \theta_r \quad (13)$$

$$I_{i+1} = (1 - \exp(-k_{i+1} \Delta x)) I_b + \exp(-k_{i+1} \Delta x) I_i \quad (14)$$

where $I_b = \frac{\sigma T_{gas}^4}{\pi}$

In order to compute the radiative intensity with Equation (14), the gas temperature T_{gas} , used to compute the blackbody intensity I_b , and the gas absorption coefficient k_{i+1} were obtained from the simulations. These two parameters were extracted along one ray from wall across from the radiometer to the inlet of the radiometer.

While a cooled target was used on the wall opposite the radiometer to reduce the radiation from the reactor wall, ash built up on the target surface during the experiments, so the condition of this surface was unknown. To compute I_o , the intensity of the target, the wall temperature from the simulation was used, and the emissivity of this surface, $\varepsilon_{cold_target}$, was taken as other parameter for the instrument model. Because of the unknown surface condition of the three cooled targets and the strong effect of the target emissivity on the radiometer measurements, the target in each section (1, 2, and 3) was assumed to have a different $\varepsilon_{cold_target}$. Therefore, this instrument model had five parameters.

$$I_o = \varepsilon_{cold_target} \frac{\sigma T_{wall}^4}{\pi} \quad (15)$$

Figure 10 compares the experimental radiometer measurements (points connected by the dotted line) with the results from the eight simulation cases in this study. The uncertainty ranges for the experimental data were obtained by applying equations (13) and (14) to the radiometer calibration with a black body. For the simulation data, the maximum values correspond to the case where the emissivity of the cooled target was assumed to be 1 and the wall temperature was equal to the simulated wall temperature. The minimum values correspond to the case where the emissivity was 0.

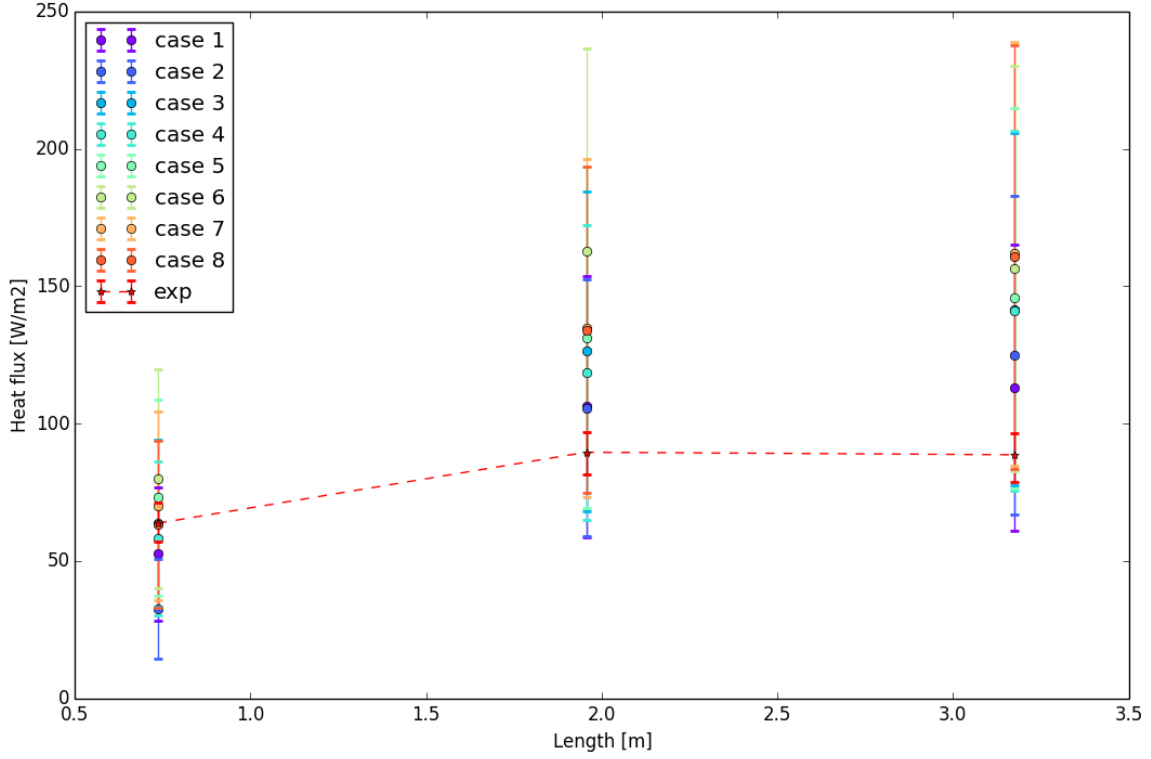


Figure 10: Comparison of experimental and simulation radiative heat flux measurements in sections 1, 2, and 3 of the L1500.

3.3 Consistency Analysis for the Thermocouple and Radiometer Measurements

A consistency analysis (described in Section 2.8) was performed using the thermocouple temperature and the radiative heat flux measurements as QOIs and $\frac{1}{R}$, v_{hiT} , and $\varepsilon_{tc}/\varepsilon_{cold_target}$ as parameters. The combined dataset included five thermocouple values and three radiometer measurements for a total of eight QOIs. The total number of parameters is six ($\frac{1}{R}$, v_{hiT} , ε_{tc} , $\varepsilon_{1,cold_target}$, $\varepsilon_{2,cold_target}$, $\varepsilon_{3,cold_target}$), two from the simulation and four from the instrument models.

The instrument models for the thermocouple and for the radiometer were used to produce 64 cases using the original eight cases presented in Table 1 and eight emissivity values between 0.0 and 1.0 for each of the four emissivity parameters. To test for consistency, a surrogate model for each QOI was created using a Gaussian Process with the 64 cases and the six parameters. These surrogate models were then used to compare with the experimental data.

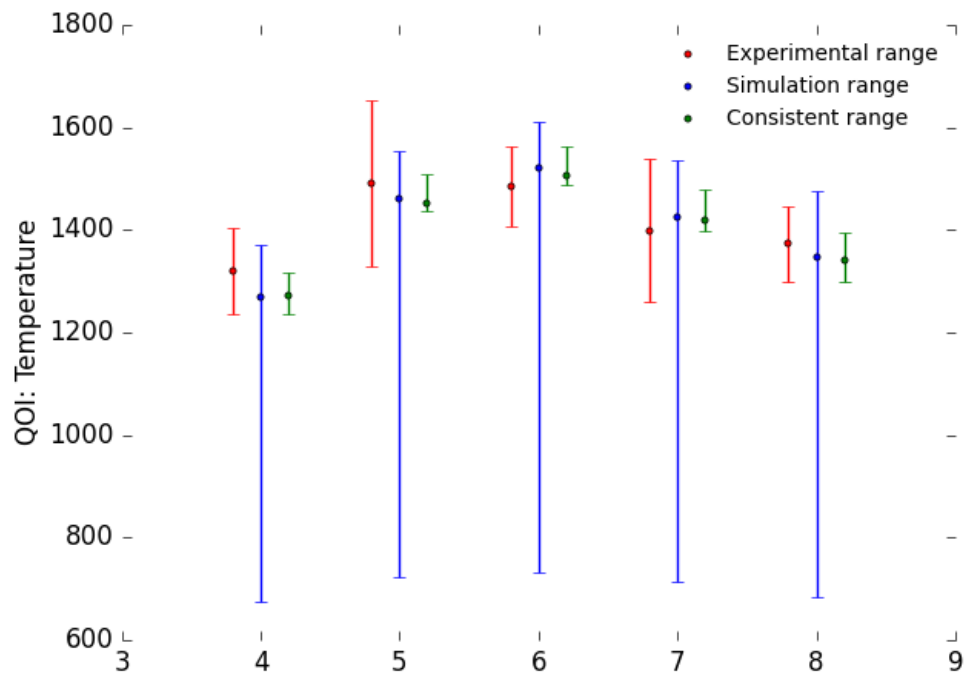
To perform the consistency analysis, the average values and uncertainty of the experimental data were required. All of the averages were computed over a five-minute window. The uncertainty of the radiometer measurements was approximated from an analysis of the radiometer calibration data with a black body.

The uncertainty for the thermocouple measurements was approximated from the scaled standard deviation for a five-minute window, assuming a distribution for the error and a 90% confidence interval. For the first three locations, the scaling factor was 30. For the last two locations, the scaling factor was 60. The factor was applied because, based on experience, the errors in the thermocouple measurements were not reflected in the measured standard deviations of 1 K. Also, without a larger experimental error range, there was no consistency between experimental and simulation data. The factor was larger for the last two points because those thermocouples were not calibrated prior to the experimental campaign. These input values for all the QOIs are listed in Table 5.

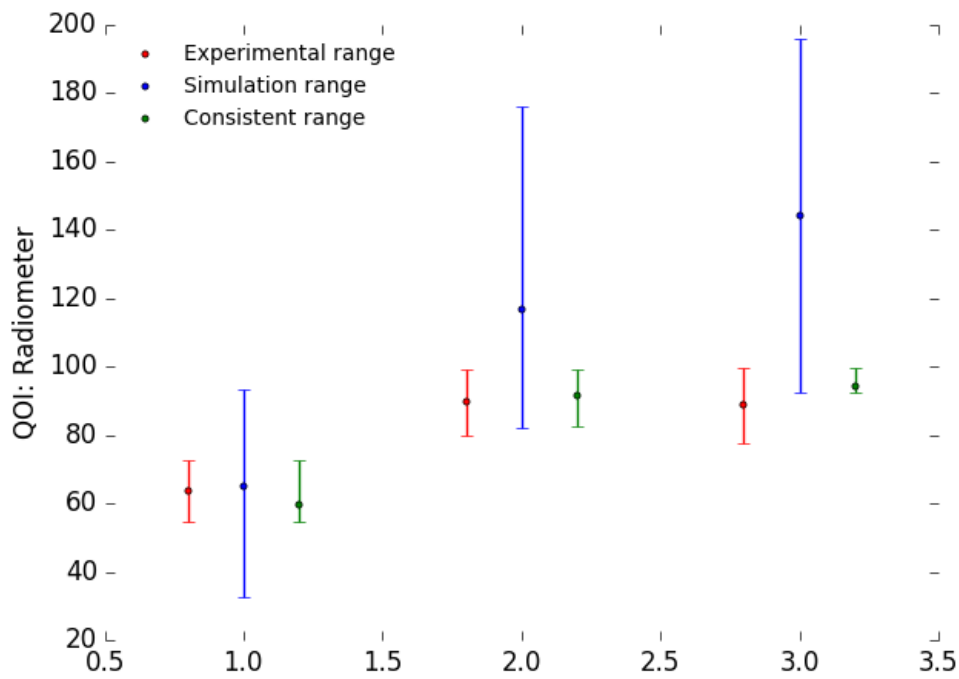
Table 5. Inputs to the consistency analysis.

QOI	Average Value	Uncertainty	Units
Radiometer 1	63.76	8.98	[W/m ²]
Radiometer 2	89.59	9.74	[W/m ²]
Radiometer 3	88.66	11.11	[W/m ²]
Thermocouple 1	1319.38	83.65	[K]
Thermocouple 2	1491.52	161.93	[K]
Thermocouple 3	1484.35	78.20	[K]
Thermocouple 4	1399.27	138.71	[K]
Thermocouple 5	1373.11	73.30	[K]

Using the inputs in Table 5 and the surrogate model previously described, an initial Monte-Carlo sampling of the parameter space was made with 10,000 points to find a consistent region. This consistent region was then sub-sampled with an additional 10,000 points to better identify its shape. The results of the analysis are presented in Figure 11(a) for the thermocouple measurements and Figure 11(b) for radiometer measurements. The figure includes the uncertainty ranges for the simulation data and the experimental data as well as the consistent region between the two datasets. The uncertainty range for the simulation is large due to the size of the parameter space that was explored. The parameter range was chosen to be large in order to encompass all the experimental data within the uncertainty of the simulation outputs. By requiring consistency between the experiment and simulation, the uncertainty range is greatly reduced for both datasets.



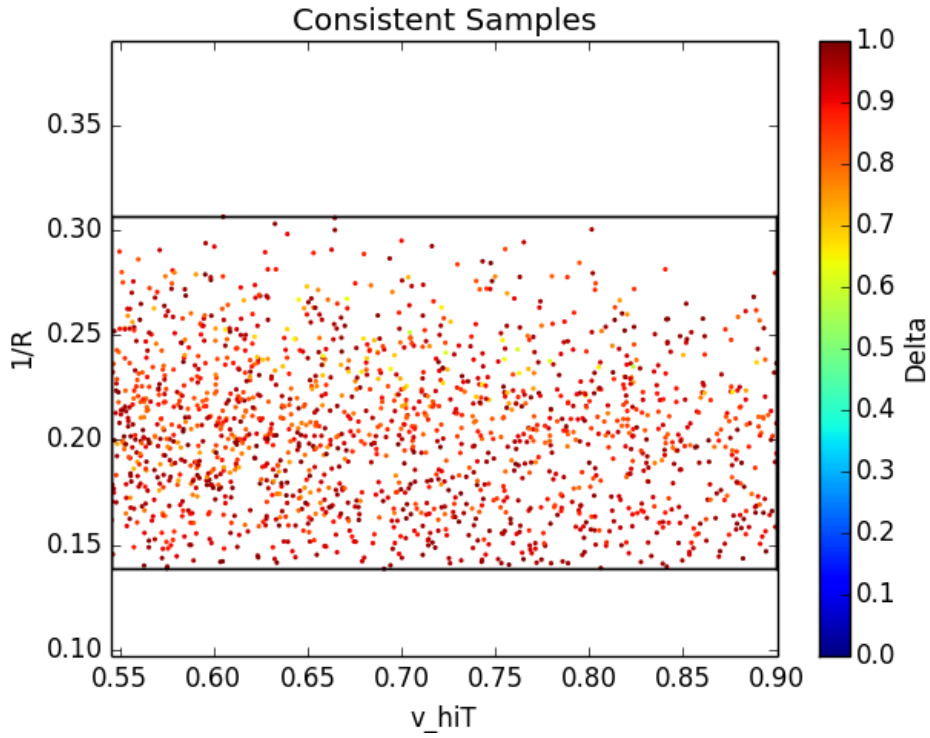
a)



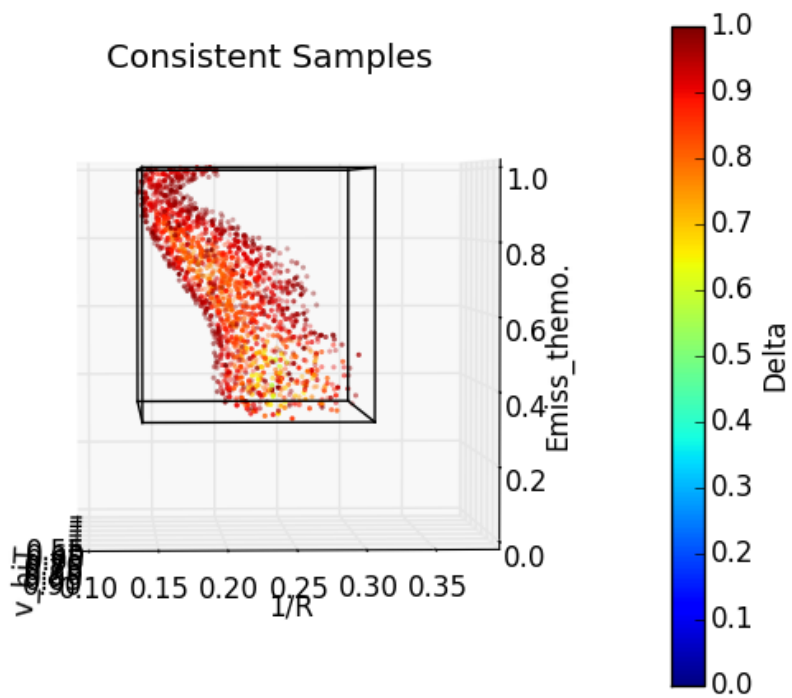
b)

Figure 11: Results of consistency analysis: (a) Thermocouple measurements, (b) radiometer measurements.

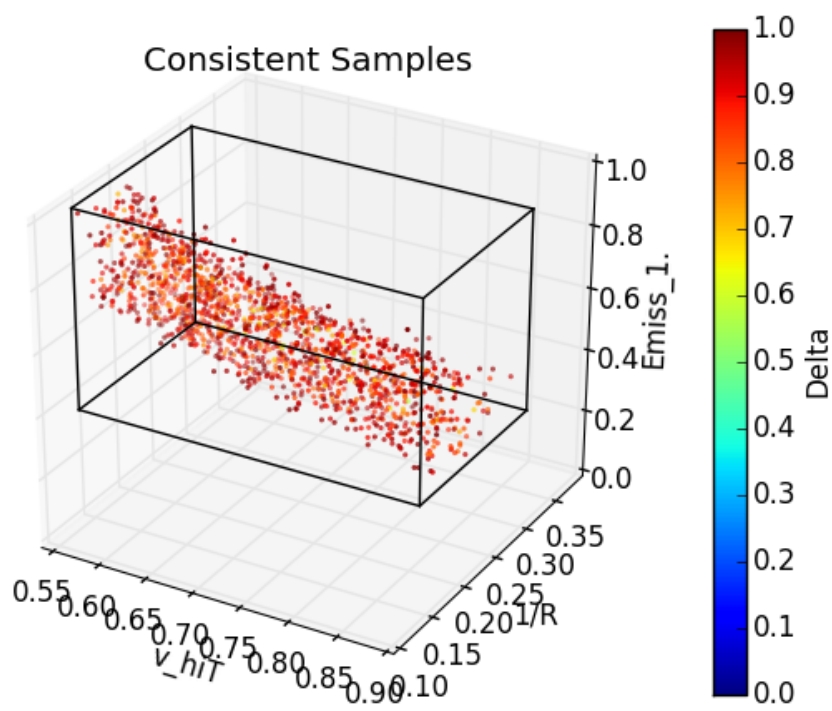
Figure 12 shows the region of parameter space (“consistent sample”) where consistency is achieved with experimental and simulation data. In these plots the color of each point is a normalized value of the discrepancy (u_e in equation (11)). The boxes represent the bounds of the parameter space containing the consistent region. While the parameter space has been reduced compared to the original parameter space (represented by the axes of the grid), some of the parameter ranges are still large. For example, the original range for ε_{tc} was reduced from 0–1 to 0.4–1. Also of note in Figure 12 are the strong correlations between some of the parameters such as $\frac{1}{R}$ and ε_{tc} in Figure 12(a).



a)



b)



c)

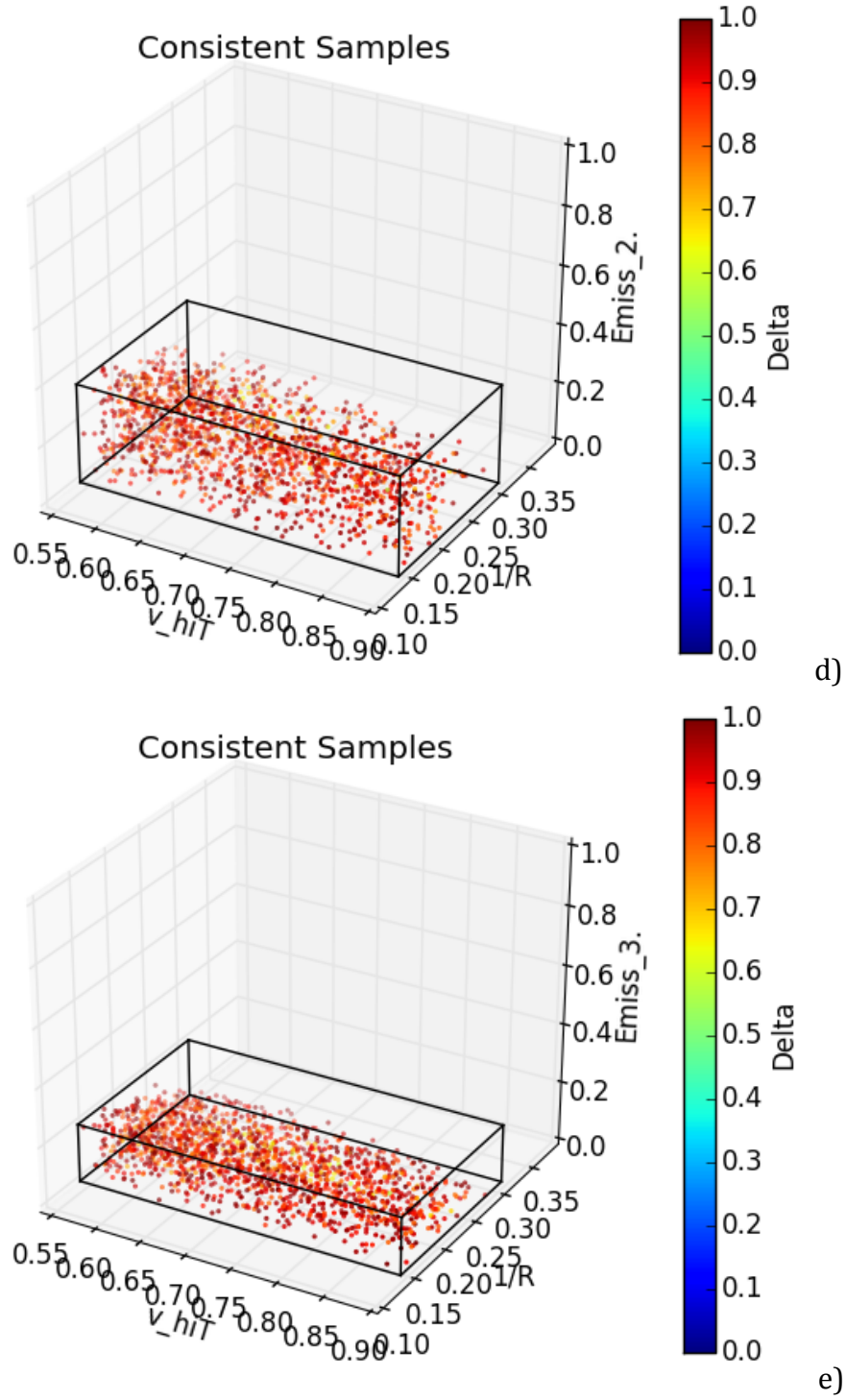


Figure 12: Consistent space for thermocouple and radiometer measurements. (a) $\frac{1}{R}$ and v_{hiT} for all emissivities, (b) $\frac{1}{R}$, v_{hiT} and ε_{tc} , (c) $\frac{1}{R}$, v_{hiT} and $\varepsilon_{1,cold_target}$, (d) $\frac{1}{R}$, v_{hiT} and $\varepsilon_{2,cold_target}$, and (e) $\frac{1}{R}$, v_{hiT} and $\varepsilon_{3,cold_target}$.

Table 6 presents the new uncertainty bounds for the six parameters resulting from the consistency analysis. From this table, it is clear that the range for v_{hiT} does not change, ε_{tc} is similar to $\varepsilon_{1,cold_target}$, and the values $\varepsilon_{2,cold_target}$ and $\varepsilon_{3,cold_target}$ are really low. Also, the range for $\frac{1}{R}$ is reduced from 0.1–0.4 to 0.14–0.30.

Table 6. Consistent parameter ranges found using uncertainties from Table 5.

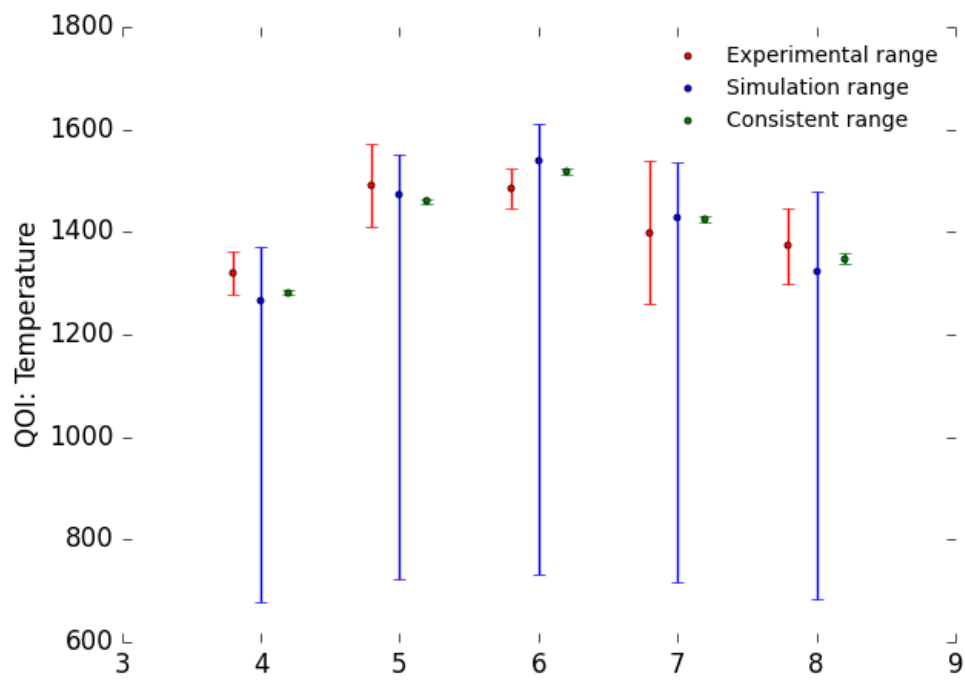
Parameter	Minimum	Maximum
v_{hiT}	0.545	0.900
$\frac{1}{R}$	0.139	0.306
ε_{tc}	0.320	1.00
$\varepsilon_{1,cold_target}$	0.352	0.990
$\varepsilon_{2,cold_target}$	0.00133	0.341
$\varepsilon_{3,cold_target}$	0.00565	0.203

The consistency region depends of the error bounds used in equation (11). However, the error in the thermocouple measurement is not well known. In order to see the impact of the thermocouple error on the size/shape of the consistency region in Figure 12, the uncertainty range shown in Table 5 was reduced for thermocouples 1, 2, and 3. For these first three locations, the scaling factor applied to the standard deviation was reduced from 30 to 15. The scaling factor (60) was not reduced for the last two locations based on the lack of calibration data for those two thermocouples. The new uncertainty bounds are given in Table 7.

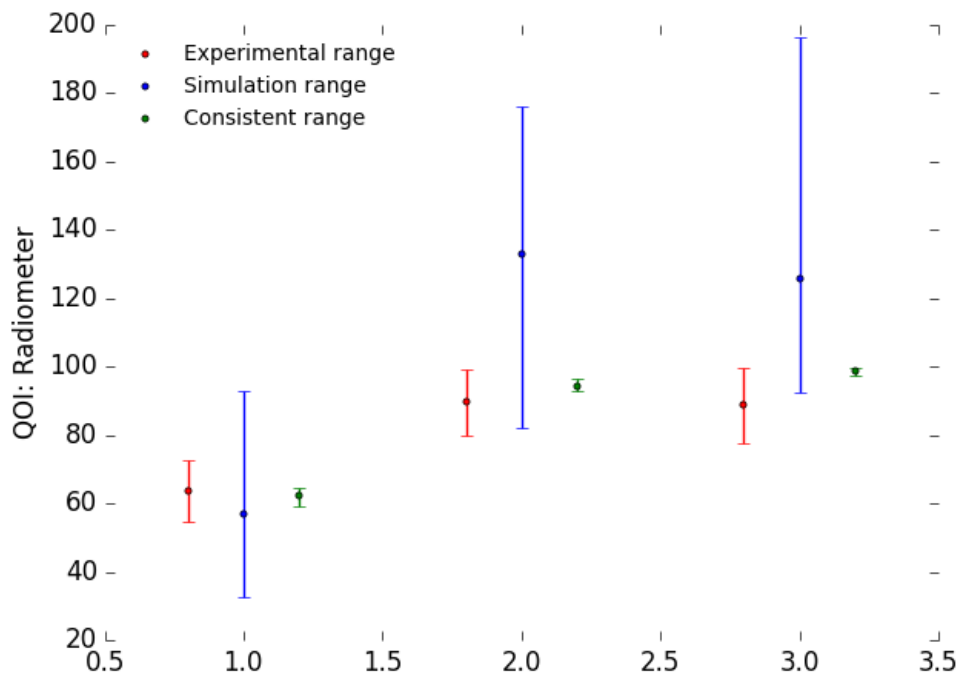
Table 7. Inputs to the consistency analysis with reduced uncertainty range for thermocouples 1, 2, and 3.

QOI	Average Value	Uncertainty	Units
Radiometer 1	63.76	8.98	[W/m ²]
Radiometer 2	89.59	9.74	[W/m ²]
Radiometer 3	88.66	11.11	[W/m ²]
Thermocouple 1	1319.38	41.83	[K]
Thermocouple 2	1491.52	80.96	[K]
Thermocouple 3	1484.35	39.09	[K]
Thermocouple 4	1399.27	138.71	[K]
Thermocouple 5	1373.11	73.30	[K]

Figure 13 and Figure 14 show the new bounds and consistent space based on the inputs in Table 7. Reducing the uncertainty by a factor of two for three of the eight QOIs reduced the consistent region to a small fraction of the original space for all six parameters. The consistent space clearly depends very strongly on the error in the thermocouple measurements. The reduced parameter ranges associated with this analysis are given in Table 8.

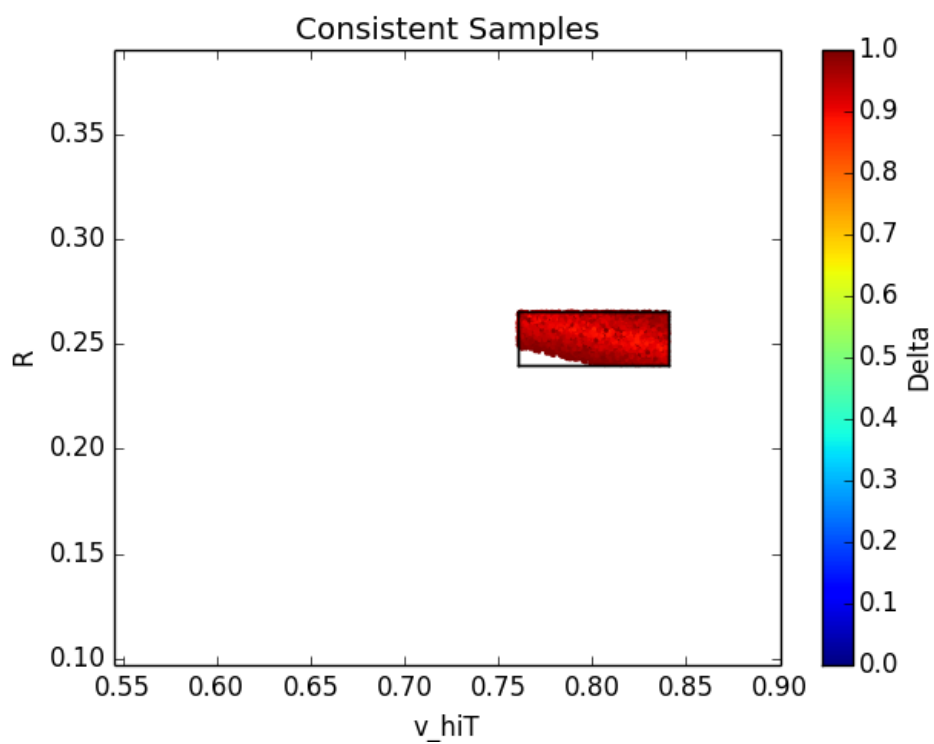


a)

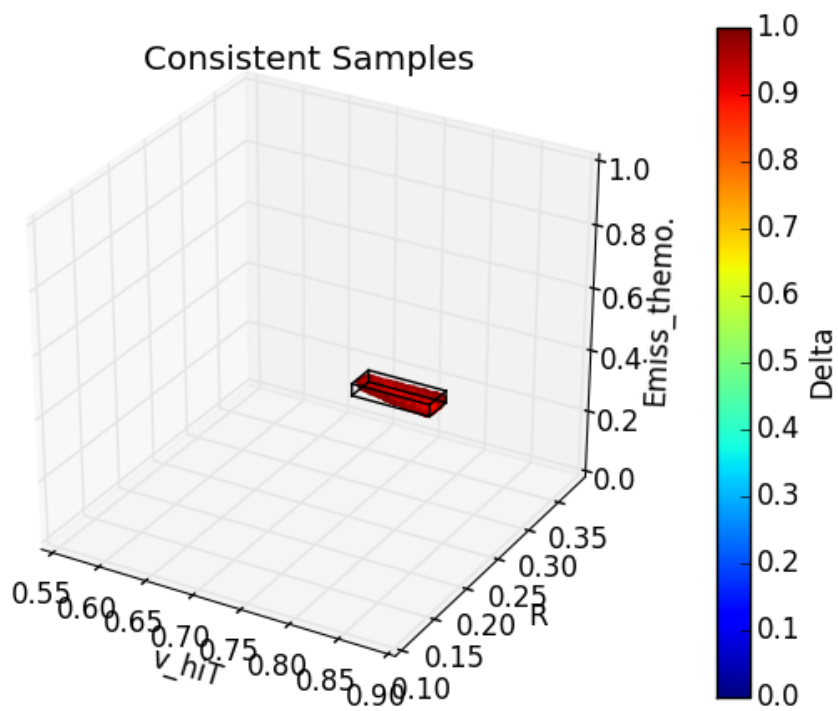


b)

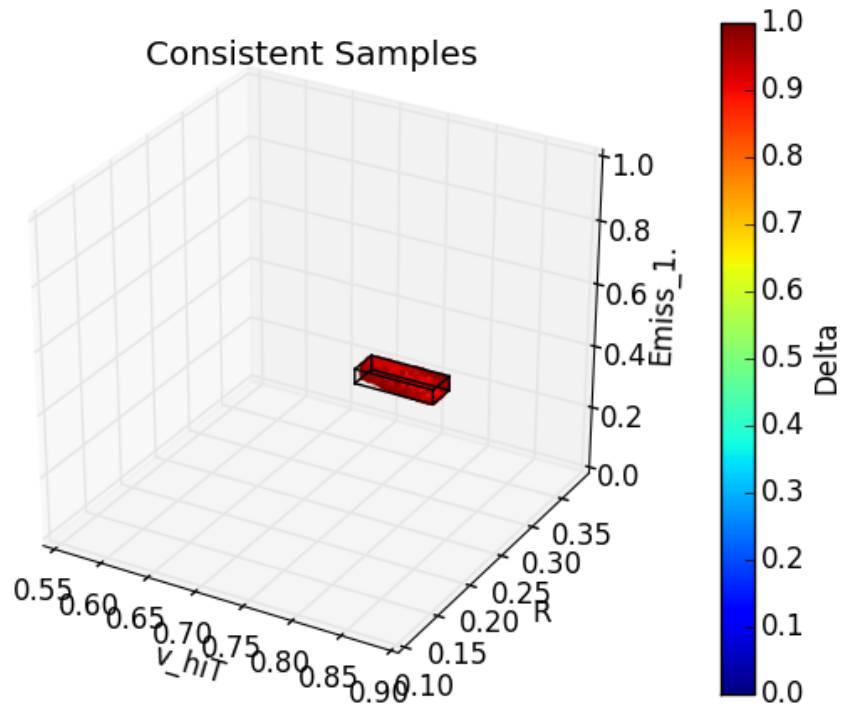
Figure 13: Results of consistency analysis: (a) Thermocouple measurements, (b) radiometer measurements



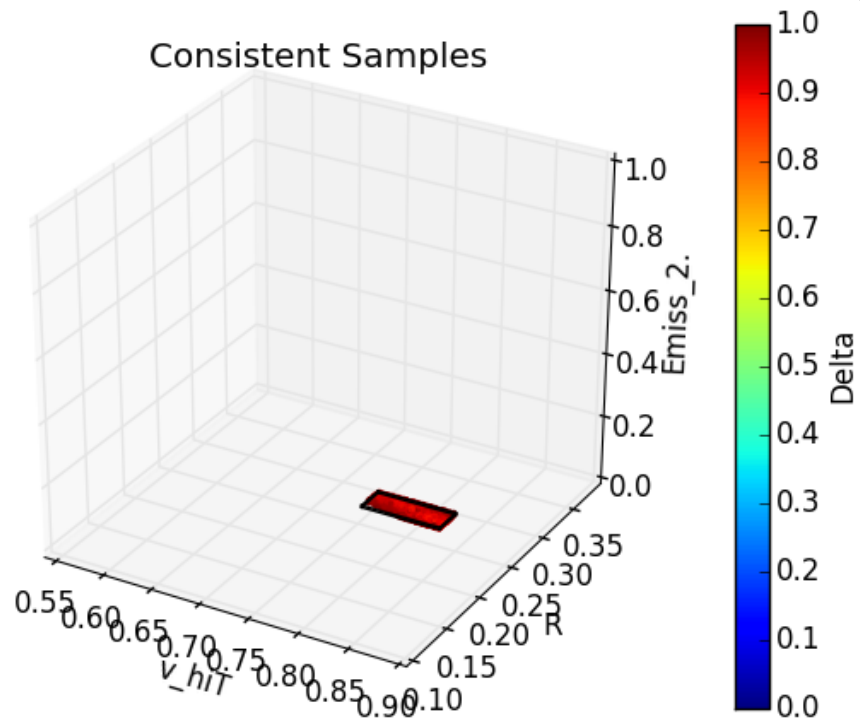
a)



b)



c)



d)

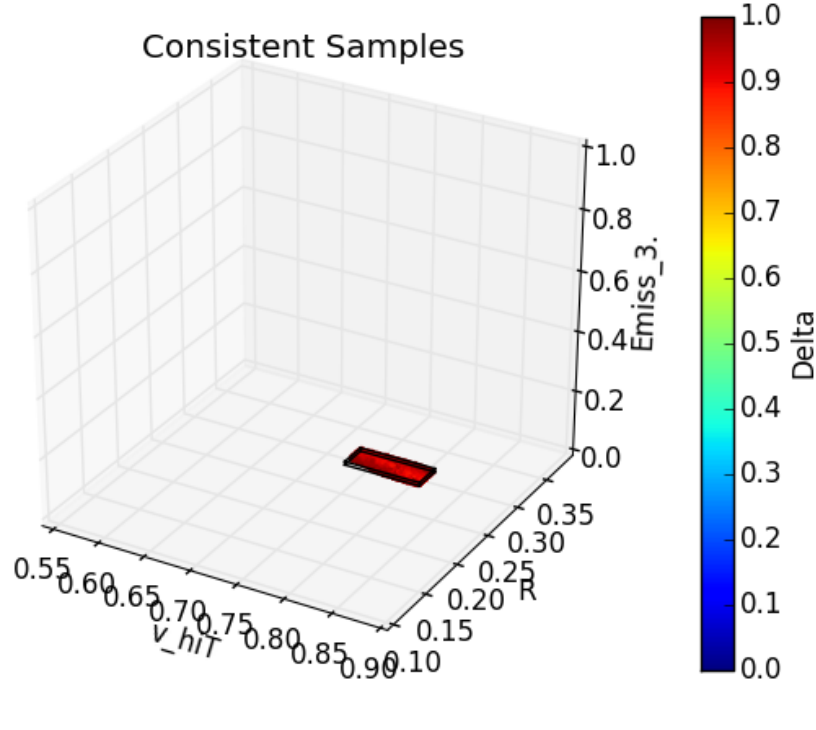


Figure 14: Consistent space for thermocouple and radiometer measurements. (a) $\frac{1}{R}$ and v_{hiT} for all emissivities, (b) $\frac{1}{R}$, v_{hiT} and ε_{tc} , (c) $\frac{1}{R}$, v_{hiT} and $\varepsilon_{1,cold_target}$, (d) $\frac{1}{R}$, v_{hiT} and $\varepsilon_{2,cold_target}$, and (e) $\frac{1}{R}$, v_{hiT} and $\varepsilon_{3,cold_target}$.

Table 8. Consistent parameter ranges found using uncertainties from Table 7.

Parameter	Minimum	Maximum
v_{hiT}	0.761	0.841
$\frac{1}{R}$	0.240	0.265
ε_{tc}	0.402	0.440
$\varepsilon_{1,cold_target}$	0.429	0.474
$\varepsilon_{2,cold_target}$	0.0602	0.0665
$\varepsilon_{3,cold_target}$	0.105	0.116

The consistency analysis shows some interesting results. First, the v_{hiT} parameter has a weaker effect than the other five parameters. Second, the ε_{tc} parameter has a value that is really close to $\varepsilon_{1,cold_target}$. Third, $\varepsilon_{2,cold_target}$ and $\varepsilon_{3,cold_target}$ values are very low. Therefore, the contribution of the radiation flux from the wall is small for sections 2 and 3 with the major radiation contribution from coming from the gas.

4. Conclusions

A VUQ analysis using a consistency method was used to study experimental and simulation data from an oxy-coal fired furnace. The dataset included eight QOIs: five thermocouple measurements and three radiometer measurements. Two simulation parameters were chosen for the analysis: a scenario parameter, $\frac{1}{R}$, and a model parameter, v_{hiT} . To look for consistency between the experimental and simulation data for the eight QOIs, it was necessary to develop two instrument models. For these instrument models, four additional parameters were studied: which the emissivity of the thermocouple, ε_{tc} , and the emissivities of the wall opposite from the radiometer, $\varepsilon_{1,cold_target}$, $\varepsilon_{2,cold_target}$, and $\varepsilon_{3,cold_target}$. Based on this analysis, it was concluded that v_{hiT} has the weakest effect on the QOIs of the six parameters tested. In the case of the parameters $\varepsilon_{2,cold_target}$, and $\varepsilon_{3,cold_target}$, low values of emissivity were obtained, which means that the contribution of the wall to the overall radiometer measurement is low and that most of the radiation comes from the gas. These low values also indicate that there was not much ash deposition on the cooled targets. Even though the emissivities of the thermocouple, ε_{tc} , and of the opposite wall in section 1, $\varepsilon_{1,cold_target}$, were not related, the values obtained for these two emissivities were similar. This result could be due to the surfaces on the cold target and on the wall thermocouple being covered with a similar particle material

For the next experimental campaign, the cold targets will be removed so as to reduce the three emissivity parameters from the study. This change will simplify the analysis. Also, because of the large sensitivity of the consistent region to the uncertainty range for thermocouple measurements in sections 1, 2, and 3, a different method with better quantified errors will be used in future experiments to measure the wall temperatures.

Acknowledgment: "This material is based upon work supported by the Department of Energy, National Nuclear Security Administration, under Award Number(s) DE-NA0002375."

Disclaimer: "This report was prepared as an account of work sponsored by an agency of the United States Government. Neither the United States Government nor any agency thereof, nor any of their employees, makes any warranty, express or implied, or assumes any legal liability or responsibility for the accuracy, completeness, or usefulness of any information, apparatus, product, or process disclosed, or represents that its use would not infringe privately owned rights. Reference herein to any specific commercial product, process, or service by trade name, trademark, manufacturer, or otherwise does not necessarily constitute or imply its endorsement, recommendation, or favoring by the United States Government or any agency thereof. The views and opinions of authors expressed

herein do not necessarily state or reflect those of the United States Government or any agency thereof."

5. References

- [1] T. Fletcher, A. Kerstein, R. J. Pugmire, M. Solum, and D. M. Grant, "A chemical percolation model for devolatilization: summary," ... *Rep. SAND92-8207*, pp. 1–66, 1992.
- [2] B. B. Schroeder, "Scale-bridging model development and increased model credibility," The University of Utah, 2015.
- [3] J. S. Justin Luitjens, John Schmidt, Alan Humphrey, J. Davison de St. Germain, Todd Harman, Jim Guilkey, Charles Reid, Dan Hinckley, Jeff Burghardt, John M. Schreiner, Joseph Peterson, Jeremy Nicholas Thornock, Brian Leavy, Qingyu Meng, Jennifer Spinti, Chuck W, "<http://www.uintah.utah.edu/>." [Online]. Available: <http://www.uintah.utah.edu/>.
- [4] J. Pedel, J. N. Thornock, and P. J. Smith, "Ignition of co-axial turbulent diffusion oxy-coal jet flames: Experiments and simulations collaboration," *Combust. Flame*, vol. 160, no. 6, pp. 1112–1128, 2013.
- [5] J. J. Murphy and C. R. Shaddix, "Combustion kinetics of coal chars in oxygen-enriched environments," *Combust. Flame*, vol. 144, no. 4, pp. 710–729, Mar. 2006.
- [6] J. Ahn, R. Okerlund, A. Fry, and E. G. Eddings, "Sulfur trioxide formation during oxy-coal combustion," *Int. J. Greenh. Gas Control*, vol. 5, pp. S127–S135, 2011.
- [7] A. Fry, B. Adams, K. Davis, D. Swensen, S. Munson, and W. Cox, "An investigation into the likely impact of oxy-coal retrofit on fire-side corrosion behavior in utility boilers," *Int. J. Greenh. Gas Control*, vol. 5, pp. S179–S185, 2011.
- [8] "<http://www.icse.utah.edu/multifuel-furnace/>." .
- [9] C. E. Rasmussen and C. K. I. Williams, *Gaussian processes for machine learning*. 2006.